Chemical and Process Engineering: New Frontiers, 2026, 47(1), e125
DOI: 10.24425/cpe.2026.158123

Influence of liquid density and viscosity differences on the development of liquid–liquid interfacial area in hydrodynamic focusing

Antoni Rożeń

Warsaw University of Technology, Faculty of Chemical and Process Engineering, Waryńskiego 1, 00-645 Warszawa, Poland

*** Corresponding author, e-mail:**
antoni.rozen@pw.edu.pl

Presented at
XIV Polish Conference
on Multiphase Flows
13–15 September 2025,
Gdańsk, Poland.
Guest Editor:
Donata Konopacka-Łyskawa

Article info:
Received: 16 September 2025
Revised: 08 January 2026
Accepted: 28 January 2026

Abstract
The development of the contact surface between mixed liquids and the reduction of striation thickness and filament diameters of the dispersed phase enable effective diffusive transport of components under stable laminar flow conditions. Hydrodynamic focusing accomplishes this at the initial mixing stage by generating viscous stresses tangential to the liquid–liquid interface and normal stresses associated with pressure. As a result, the additive stream forms either an elongated filament (3D focusing) or a thin striation (2D focusing). This work examines the influence of the physical properties of liquids and the focusing method on the intermaterial surface area concentration in vertical flow systems, where gravitational segregation is avoided. The Navier–Stokes equations were solved for the axisymmetric core–ring flow in a pipe and the stratified symmetric flow in rectangular channels of different aspect ratios. The effects of differences in liquid density and viscosity, as well as the axial pressure gradient, on the transverse size of the focused stream and the contact surface concentration were determined for both upward and downward flow. In addition, the influence of the rectangular channel geometry on the residence-time distribution of the additive liquid was analysed.

Keywords
vertical focusing flow, gravity effect, pressure gradient, liquid-liquid mixing

1. INTRODUCTION

The efficiency of mixing processes is governed by three mechanisms: macroscopic convection, which determines the residence-time distribution of fluid elements; microscopic convection, which deforms fluid structures; and molecular diffusion, which smooths concentration fluctuations. When liquid solutions of high viscosity or prone to degradation under hydrodynamic stress are brought into contact, mixing is typically carried out under laminar-flow conditions. In such systems it is challenging to achieve both a narrow residence-time distribution and a high mass-transfer rate across the liquid–liquid interface. These limitations may significantly affect the morphology of the liquid–liquid system, the chemical composition, and the physical properties of the final product. The main stage of laminar mixing can be enhanced by increasing the overall mixing power (Zlokarnik, 2001), by inducing chaotic advection (Aref, 1984; Ottino, 1989), or by improving energy efficiency (Ottino et al., 1979; Rożeń and Kopytowski, 2021). Crucially, at the dosing stage of the side stream into the main flow, the diffusion path of solutes should be minimised and the interfacial area rapidly developed. Moreover, the side stream must be introduced in a manner that reduces the residence-time spread of its elements within the system (Lu et al., 2016). This requirement is particularly critical in systems where the reaction rate is faster than, or comparable with, the molecular mixing rate, as in precipitation processes (Karnik, 2008). The objectives of the initial mixing stage may be achieved by reducing the size of the flow system (Hessel et al., 2005), splitting the additive stream into multiple smaller streams (Mansur et al., 2008), tailoring the geometry of the dosing head (Gao et al., 2021; Rahbarshahlan et al., 2021; Zhang et al., 2019), or employing hydrodynamic focusing (Chiu et al., 2013; Knight et al., 1998; Lee et al., 2006). Such methods are widely used, though not exclusively, in the design of micromixers and microreactors.

Hydrodynamic focusing shapes the additive into a thin layer or filament enveloped by the main liquid stream. This occurs as a result of tangential viscous stresses and normal stresses acting on the interface. When the liquids form immiscible phases, the final stage of focusing results in break-up of the additive into droplets (Chen et al., 2015; Wu et al., 2017). Hydrodynamic focusing serves not only to reduce the local segregation scale or to generate emulsion microdroplets but also to enlarge the interfacial area between liquids (Bothe et al., 2008; Gao et al., 2021; Rożeń and Kopytowski, 2025). These processes are closely interlinked and depend on the geometry of the premixing head, the dosing rates of the streams, and the viscosity and density of the phases (Minetti et al., 2020; Shivhare et al., 2016; Tripathi et al., 2014). Since its potential was first recognised by Knight et al. (1998), hydrodynamic focusing has found increasing application in classical chemical engineering (Jaffer and Wood, 1998), chemical microanalysis (Golden et al., 2012), rheology (Dziubinski, 2012), medicine (Weigl et al., 1999; Yamada et al., 2008), and biology (Knoška et al., 2020).

The stability of hydrodynamic focusing depends sensitively on operating conditions and may be disrupted at the very inlet by hydrodynamic instabilities. Key sources of instability include viscosity and density contrasts and the presence of interfacial tension (Joseph and Renardy, 1993). Mechanical vibrations of the apparatus and fluctuations in dosing rate must also be considered. A viscosity difference introduces a discontinuity in the velocity gradient at the interface, which alone can destabilise the flow (Bałdyga and Rożeń, 1994). Moreover, the viscosity ratio of additive to focusing liquids can strongly influence the focusing outcome (Rożeń and Kopytowski, 2025). Flow-rate fluctuations can be mitigated using gear, screw, or lobe pumps. In horizontal-flow systems, density differences cause reorientation of the interface and thus destabilise the flow or at least induce gravitational segregation (Heravi et al., 2023; Yamaguchi et al., 2006). A vertical configuration of the premixing system with gravitational dosing facilitates flow stability but simultaneously affects focusing performance (Giorello et al., 2020; Minetti et al., 2022). Specifically, it alters the thickness or radius of the additive stream relative to the values obtained for negligible density differences. When designing a hydrodynamic focusing process, it is also necessary to define whether the goal is maximum reduction of the stream's transverse dimension – so that solutes can readily diffuse and react (Karnik et al., 2008) – or rather uniform mixing of the additive across the cross-section of the main stream, which requires a narrow residence-time distribution and high interfacial area concentration in the outlet stream.

Only a limited number of studies have addressed vertical-flow micromixers, and most have focused on the geometry of streams of different densities. Stiles and Fletcher (2003; 2004) provided exact analytical and numerical solutions for the vertical flow of two liquids with different densities and viscosities in a rectangular microchannel. Giorello et al. (2020) proposed a model for vertical two-liquid flow in a micro-slit (Hele–Shaw flow). However, this simple model does not account for velocity gradients at the interface and therefore cannot accurately predict the interfacial area concentration in the product. Moreover, these works do not include residence-time distribution calculations.

The purpose of this study is to investigate the generation of interfacial area between liquids differing in density and viscosity in two fundamental types of vertical focusing systems, without simplifications to the flow description. The first system produces core – annular flow in a circular channel, with the additive forming a filament along the axis of symmetry. The second system produces symmetric flow in a rectangular channel, where the additive forms a layer along one longitudinal plane of symmetry. Accurate modelling of both focusing and focused streams makes it possible to determine the influence of density and viscosity differences on the transverse size of the additive stream (filament diameter or layer thickness) and on the interfacial area concentration per unit product volume. In addition, the influence of channel aspect ratio on the residence-time distribution is examined. Calculations are performed for a wide range of axial pressure gradients to identify conditions under which density differences affect or even prevent hydrodynamic focusing.

2. MODELLING OF FLOWS CREATED BY HYDRODYNAMIC FOCUSING

2.1. Axisymmetric core-annular flow

The process in which a liquid stream containing reagents, droplets, polymer particles, or living cells is shaped into a slender filament as it enters the main flow is known as three-dimensional (3D) hydrodynamic focusing. This operation is achieved by surrounding the additive with the main stream so that the additive forms the central core of the flow. The cross-sectional area of this core, and to some extent its shape, can be adjusted by varying the flow-rate ratio of the focusing and focused streams (Chiu et al., 2013; Huyke et al., 2020; Kennedy et al., 2011; Lu et al., 2014; Minetti et al., 2022). An ideally axisymmetric focused stream is most readily obtained by injecting the additive centrally into the main liquid through a nozzle, as illustrated in Fig. 1. The main stream, of density ρ_1 and viscosity μ_1, flows through a channel of radius R. The additive, of density ρ_2 and viscosity μ_2, is introduced along the axis and, as a result of focusing, forms a filament of radius r_s. The volumetric flow rates are Q_1 for the focusing stream and Q_2 for the focused stream.

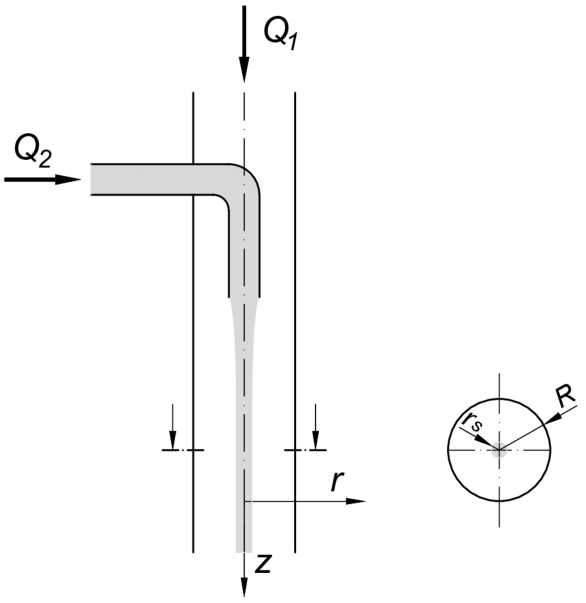

Figure 1. Hydrodynamic focusing in axisymmetric core–annular flow.

The analysis presented below is restricted to a stable, fully developed laminar flow regime downstream of the injection region. In this regime, hydrodynamic focusing is preserved, and no interfacial instabilities are observed.

Once the flow is stabilised downstream of the injection point, the velocity vectors of both liquids have only axial components: v_1 for the main stream and v_2 for the additive. With vertical orientation, the Navier–Stokes equations reduce to:

$$0 = -\frac{\partial p}{\partial z} \pm \rho_1 g + \mu_1 \frac{1}{r}\frac{\partial}{\partial r}\left(r\frac{\partial v_1}{\partial r}\right) \tag{1}$$

$$0 = -\frac{\partial p}{\partial z} \pm \rho_2 g + \mu_2 \frac{1}{r}\frac{\partial}{\partial r}\left(r\frac{\partial v_2}{\partial r}\right) \tag{2}$$

The plus sign in the gravitational term corresponds to downward flow, while the minus sign denotes upward flow, as the orientation of the z-axis coincides with the flow direction. The velocity profile in axisymmetric flow must satisfy the following boundary conditions:

a) no-slip at the channel wall

$$v_1|_{r=R} = 0 \tag{3}$$

b) velocity continuity at the liquid–liquid interface

$$v_1|_{r=r_s} = v_2|_{r=r_s} \tag{4}$$

c) continuity of shear stress across the liquid–liquid interface

$$\mu_1 \left.\frac{\partial v_1}{\partial r}\right|_{r=r_s} = \mu_2 \left.\frac{\partial v_2}{\partial r}\right|_{r=r_s} \tag{5}$$

d) zero velocity gradient at the axis of symmetry

$$\left.\frac{\partial v_2}{\partial r}\right|_{r=0} = 0 \tag{6}$$

Because the liquid–liquid interface is aligned with the flow direction and the velocity field is purely axial, capillary forces act in the transverse direction and do not contribute to the axial stress balance at the interface. Consequently, interfacial tension does not appear explicitly in the boundary condition for the axial component of the stress in Eq. (5).

The solution of Eqs. (1)–(6) can be expressed as:

$$\begin{aligned} v_1(r) = {} & \left(-\frac{\partial p}{\partial z} \pm \rho_1 g\right)\frac{R^2 - r^2}{4\mu_1} \\ & \pm \frac{(\rho_1 - \rho_2)\, g r_s^2}{2\mu_1} \ln\left(\frac{r}{R}\right) \end{aligned} \tag{7}$$

$$\begin{aligned} v_2(r) = {} & \left(-\frac{\partial p}{\partial z} \pm \rho_2 g\right)\frac{r_s^2 - r^2}{4\mu_2} \\ & + \left(-\frac{\partial p}{\partial z} \pm \rho_1 g\right)\frac{R^2 - r_s^2}{4\mu_1} \\ & \pm \frac{(\rho_1 - \rho_2)\, g r_s^2}{2\mu_1} \ln\left(\frac{r_s}{R}\right), \end{aligned} \tag{8}$$

By integrating the velocity profiles in (7) and (8), the volumetric flow rates of the two streams are obtained as:

$$\begin{aligned} Q_1 = {} & \left(-\frac{\partial p}{\partial z} \pm \rho_1 g\right)\frac{\pi\left(R^2 - r_s^2\right)^2}{8\mu_1} \\ & \pm \frac{(\rho_1 - \rho_2)\, g \pi r_s^2}{4\mu_1}\left\{-R^2 - r_s^2\left[2\ln\left(\frac{r_s}{R}\right) - 1\right]\right\} \end{aligned} \tag{9}$$

$$\begin{aligned} Q_2 = {} & \left(-\frac{\partial p}{\partial z} \pm \rho_2 g\right)\frac{\pi r_s^4}{8\mu_2} \\ & + \left(-\frac{\partial p}{\partial z} \pm \rho_2 g\right)\frac{r_s^2\left(R^2 - r_s^2\right)}{4\mu_1} \\ & \pm \frac{(\rho_1 - \rho_2)\, g \pi r_s^4}{2\mu_1} \ln\left(\frac{r_s}{R}\right) \end{aligned} \tag{10}$$

The concentration of interfacial area in the mixture volume produced by the focusing system is defined as:

$$a_V = \frac{2\pi r_s v_s}{Q_1 + Q_2} \tag{11}$$

where $v_s = v_1(r_s)$ is the velocity at the interface.

In the fully developed laminar flow considered here, transverse velocity components vanish, and axial velocity gradients are negligible. Momentum transfer between adjacent fluid layers is therefore governed by viscous diffusion, and nonlinear convective terms in the momentum equations are absent. As a result, the Reynolds number does not influence the shape of the axial velocity profiles described by Eqs. (7)–(10).

Analysis of Eqs. (9) and (10) indicates that the ratio r/R depends on four dimensionless parameters:

- the volumetric flow-rate ratio:

$$F = Q_1/Q_2 \tag{12}$$

- the density ratio ρ_2/ρ_1, the viscosity ratio μ_2/μ_1, and the ratio of the actual pressure gradient to the hydrostatic gradient:

$$P = \left(\frac{\partial p}{\partial z}\right)\frac{1}{\rho_1 g} \tag{13}$$

With the ratio r_s/R known, the ratio of the interfacial velocity to the mean channel velocity, $v_s/\overline{v}$, can be calculated, along with the product of the interfacial area concentration and the hydraulic diameter (Eq. (14)).

$$a_V d_h = \frac{2\pi r_s v_s}{\pi R^2 \overline{v}} 2R = 4\frac{r_s}{R}\cdot\frac{v_s}{\overline{v}} \tag{14}$$

Because of the nonlinear nature of Eqs. (9) and (10), the Levenberg–Marquardt method was used to determine the ratio of the additive filament radius to the channel radius (Press et al., 1992). Calculations were carried out for liquids differing in density and either equal or different viscosities, at a volumetric ratio $F = 10$.

The applicability of the present model is therefore limited to conditions for which hydrodynamic focusing remains stable, i.e.

Reynolds numbers of order 10 or lower (Cubaud and Notaro, 2014) and capillary numbers sufficiently large (at least 0.1 or higher) to suppress interfacial destabilisation, as reported in the literature (Cubaud and Mason, 2008). Outside this range, flow instabilities may develop, and the assumptions underlying the present analysis become invalid. The Reynolds number, necessary to determine the flow regime, can be defined using the method proposed by Metzner and Reed (1955), which is based on the use of the laminar flow resistance law for flow through a channel

$$\mathrm{Re} = \frac{32}{\pm\overline{\rho}g - \left(\frac{\partial p}{\partial z}\right)} \cdot \frac{\overline{\rho}\,\overline{v}^2}{d_h} \tag{15}$$

The plus sign in (15) denotes downward flow, while the minus sign denotes upward flow. The average liquid density and velocity are calculated as follows:

$$\overline{\rho} = \frac{F + \rho_2/\rho_1}{F+1}\rho_1 \tag{16}$$

$$\overline{v} = \frac{Q_1 + Q_2}{A} \tag{17}$$

where A is the cross-sectional area of the channel. On the other hand, the capillary numbers for each liquid can be defined using the work of Cubaud and Mason (2008).

Introducing modified pressure

$$\tilde{p} = p \mp \overline{\rho} g z \tag{18}$$

into Eq. (15) allows relating the Reynolds number to the Euler number

$$\mathrm{Re} = 32\frac{L}{d_h} \cdot \frac{\overline{\rho}\,\overline{v}^2}{-\left(\frac{\partial \tilde{p}}{\partial z}\right) L} = 32\frac{L}{d_h} \cdot \frac{1}{\mathrm{Eu}} \tag{19}$$

where L is the channel length. On the other hand, introducing a new dimensionless parameter

$$\varepsilon = \pm 1 - \left(\frac{\partial p}{\partial z}\right)\frac{1}{\overline{\rho}g} = \pm 1 - P\frac{F+1}{F+\rho_2/\rho_1} \tag{20}$$

allows relating the Reynolds number to the Froude number

$$\mathrm{Re} = \frac{32}{\varepsilon} \cdot \frac{\overline{v}^2}{g d_h} = \frac{32}{\varepsilon}\mathrm{Fr} \tag{21}$$

Expressing the operating conditions in terms of Reynolds, Euler, and Froude numbers allows the present results to be transferred from micro- and laboratory-scale systems to larger continuous flow devices, provided that dynamic similarity is maintained. Beyond micro- and millimetre-scale systems, hydrodynamic focusing in axisymmetric configurations can also be of practical relevance for centimetre-scale continuous-flow reactors and contactors. In particular, it is advantageous in applications where the additive stream is chemically aggressive, highly viscous, or prone to deposition on solid surfaces. In such cases, the main stream acts as a hydrodynamic barrier, shielding the channel walls from direct contact with the additive, stabilising the position of the focused core. This protective effect provides an additional motivation for implementing hydrodynamic focusing in larger-scale flow devices.

The parameter ε, defined by Eq. (20), is always positive, with smaller values obtained when pressure losses due to viscous resistance are minimised. Changes in ε directly reflect variations in the actual pressure gradient relative to the hydrostatic gradient. The minimum ε occurs when any further adjustment of the pressure gradient (an increase in downward flow or a decrease in upward flow) prevents maintaining the prescribed volumetric flow-rate ratio F.

The resulting values of r_s/R and $a_V d_h$ are shown in Figs. 2 and 3 as functions of the parameter ε. Analysis of the these results indicates that, irrespective of whether the focusing flow is directed downward or upward, both the radius of the additive stream and the interfacial area concentration vary with decreasing ε. These variations are negligible for $\varepsilon \gg 1$ but become pronounced once $\varepsilon < 1$. From a design perspective, these results provide direct guidelines for selecting the flow direction and the axial pressure gradient relative to the hydrostatic gradient to maximise interfacial area development for given density and viscosity contrasts.

For downward flow (Figs. 2a–c and 3a–c), when the additive is denser than the focusing liquid ($\rho_2 > \rho_1$), reducing ε narrows the additive filament and increases the interfacial velocity. Consequently, the interfacial area concentration rises. The closer the system is to the minimum ε that still allows the prescribed flow-rate ratio to be maintained, the greater the interfacial area development. It should be emphasised that this limiting ε grows with the additive-to-main-stream density ratio. The viscosity ratio has only a minor influence on the limiting ε, yet, with other parameters unchanged, a higher viscosity yields a noticeable increase in interfacial area concentration.

For downward flow with a lighter additive ($\rho_2 < \rho_1$), a reduction in ε expands the additive stream radius because the mean velocity of the focused liquid decreases. In this case, whether the interfacial area concentration increases or decreases depends on the viscosity ratio. If $\mu_2 < \mu_1$, the concentration rises as ε decreases (Fig. 3a), whereas for $\mu_2 \geq \mu_1$, it falls with decreasing ε (Figs. 3b–c).

For upward flow (Figs. 2d–f and 3d–f), the density ratio has the opposite effect on the additive radius and interfacial area compared with downward flow. Nevertheless, the general shape of the ε-dependence curves is similar to that obtained for downward flow. Importantly, however, the direction of flow influences the minimum ε values. As shown in Tables 1–3, the greater the density ratio exceeds unity, the smaller the $\varepsilon_{\min}$ values for upward flow compared with the downward case.

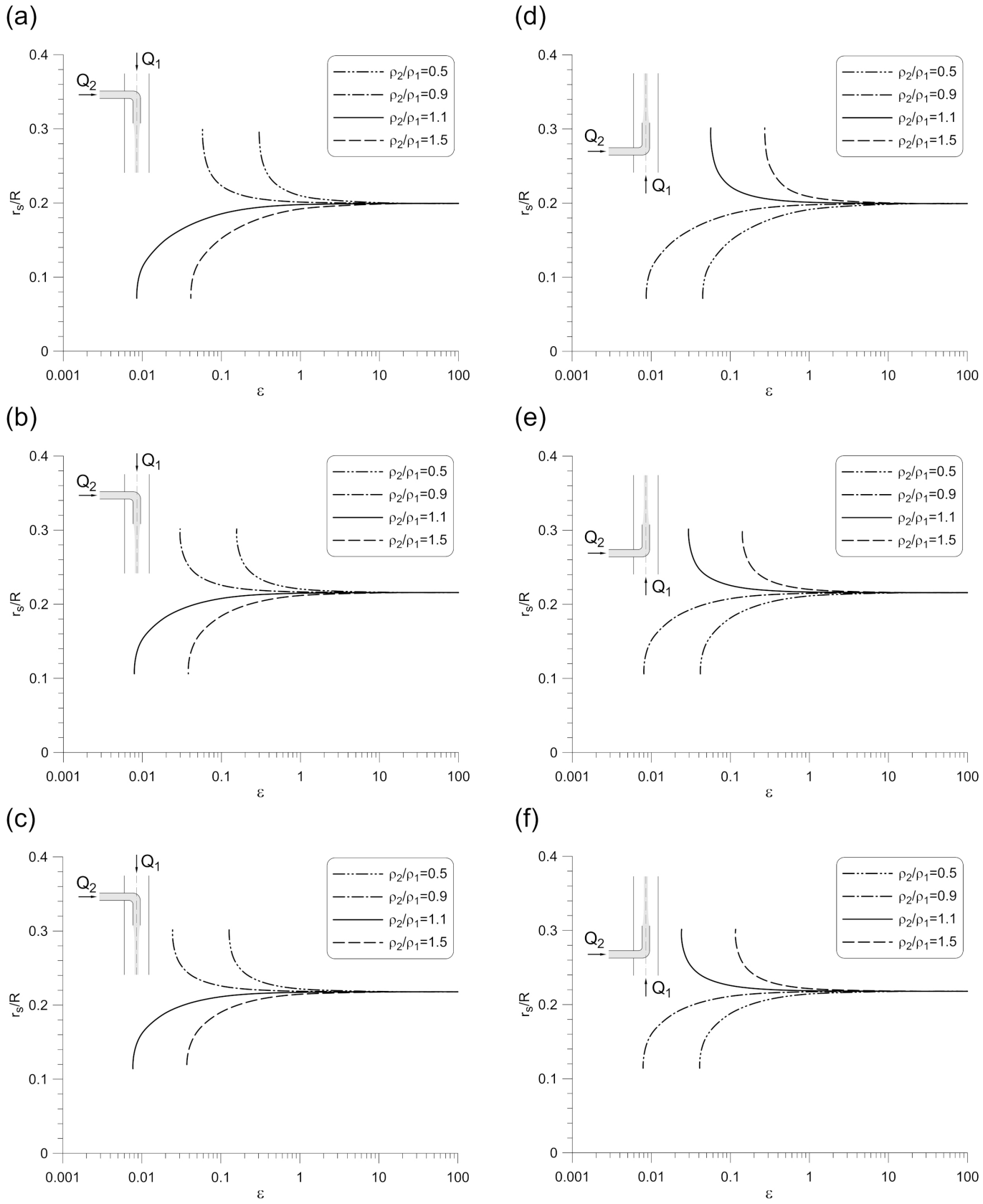

Figure 2. Effect of the density and viscosity ratio on the relative radius of the additive stream in vertical core–annular flow ($F = 10$): (a) downward flow, $\mu_2/\mu_1 = 0.1$; (b) downward flow, $\mu_2/\mu_1 = 1$; (c) downward flow, $\mu_2/\mu_1 = 10$; (d) upward flow, $\mu_2/\mu_1 = 0.1$; (e) upward flow, $\mu_2/\mu_1 = 1$; (f) upward flow, $\mu_2/\mu_1 = 10$.

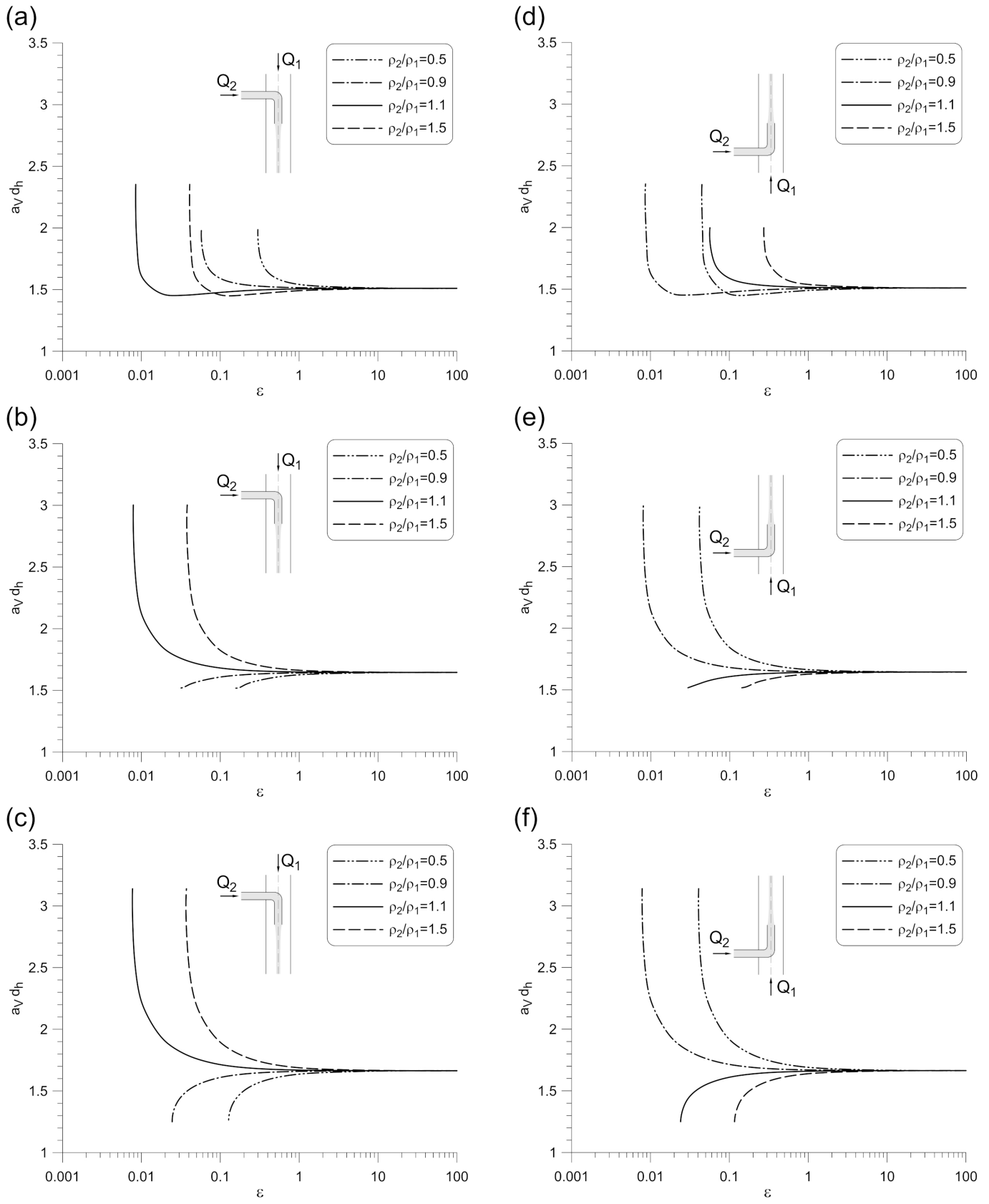

Figure 3. Effect of the density and viscosity ratio on the dimensionless interfacial area concentration in vertical core–annular flow ($F = 10$): (a) downward flow, $\mu_2/\mu_1 = 0.1$; (b) downward flow, $\mu_2/\mu_1 = 1$; (c) downward flow, $\mu_2/\mu_1 = 10$; (d) upward flow, $\mu_2/\mu_1 = 0.1$; (e) upward flow, $\mu_2/\mu_1 = 1$; (f) upward flow, $\mu_2/\mu_1 = 10$.

Table 1. Limiting values of parameter ε for core-annular flow; $F = 10$, $\mu_2/\mu_1 = 0.1$.

Downward flow	ρ_2/ρ_1	1.1	1.2	1.3	1.4	1.5	2
	ε_{min}	0.00850	0.01685	0.02506	0.03312	0.04103	0.07865
Upward flow	ρ_1/ρ_2	1.1	1.2	1.3	1.4	1.5	2
	ε_{min}	0.00786	0.01452	0.02022	0.02517	0.02949	0.04494

Table 2. Limiting values of parameter ε for core-annular flow; $F = 10$, $\mu_2/\mu_1 = 1$.

Downward flow	ρ_2/ρ_1	1.1	1.2	1.3	1.4	1.5	2
	ε_{min}	0.00789	0.01565	0.02326	0.03074	0.03809	0.07301
Upward flow	ρ_1/ρ_2	1.1	1.2	1.3	1.4	1.5	2
	ε_{min}	0.00730	0.01348	0.01878	0.02336	0.02738	0.04172

Table 3. Limiting values of parameter ε for core-annular flow; $F = 10$, $\mu_2/\mu_1 = 10$.

Downward flow	ρ_2/ρ_1	1.1	1.2	1.3	1.4	1.5	2
	ε_{min}	0.00772	0.01530	0.02274	0.03006	0.03725	0.07139
Upward flow	ρ_1/ρ_2	1.1	1.2	1.3	1.4	1.5	2
	ε_{min}	0.00714	0.01318	0.01836	0.02284	0.02677	0.04080

2.2. Symmetric stratified flow

The process in which an additive stream is formed into a flat layer at a defined position and orientation within the channel cross-section is known as two-dimensional (2D) hydrodynamic focusing. This configuration can be achieved, for instance, by splitting the main flow into two side streams that confine the additive from opposite sides, thereby flattening and narrowing it within a rectangular channel (Fig. 4). The thickness of the additive layer and the degree of flow symmetry can be controlled by adjusting the dosing rates of the individual streams entering the focusing head (Giorello et al., 2020; Lee et al., 2006; Tripathi et al., 2014). After the flow stabilises downstream of the focusing region, both liquids exhibit purely axial velocity components (v_1 and v_2). The Navier–Stokes equations describing this configuration then take the form:

$$0 = -\frac{\partial p}{\partial z} \pm \rho_1 g + \mu_1 \left(\frac{\partial^2 v_1}{\partial x^2} + \frac{\partial^2 v_1}{\partial y^2} \right) \tag{22}$$

$$0 = -\frac{\partial p}{\partial z} \pm \rho_2 g + \mu_2 \left(\frac{\partial^2 v_2}{\partial x^2} + \frac{\partial^2 v_2}{\partial y^2} \right) \tag{23}$$

The plus sign in the gravitational term corresponds to downward flow, while the minus sign denotes upward flow, since the z-axis is aligned with the flow direction. The velocity distribution in symmetric flow through a channel of width w and height h, with a central additive stream of thickness w_s, must satisfy the following boundary conditions:

- no-slip at the channel walls

$$v_1|_{x=\pm w/2} = v_1|_{y=\pm h/2} = v_2|_{y=\pm h/2} = 0 \tag{24}$$

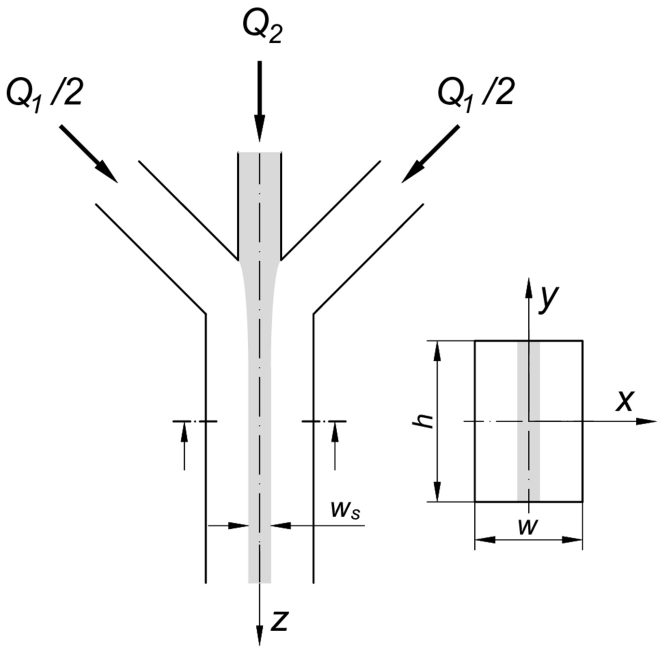

Figure 4. Two-dimensional hydrodynamic focusing: symmetric stratified flow in a rectangular channel.

- velocity continuity at the liquid–liquid interface

$$v_1|_{x=\pm w_s/2} = v_2|_{x=\pm w_s/2} \tag{25}$$

- continuity of shear stress across the liquid–liquid interface

$$\mu_1 \left. \frac{\partial v_1}{\partial x} \right|_{x=\pm w_s/2} = \mu_2 \left. \frac{\partial v_2}{\partial x} \right|_{x=\pm w_s/2} \tag{26}$$

- zero velocity gradient along the channel mid-plane (yz-plane)

$$\left.\frac{\partial v_2}{\partial x}\right|_{x=0} = 0 \tag{27}$$

- zero velocity gradient along the central plane (xz-plane)

$$\left.\frac{\partial v_1}{\partial y}\right|_{y=0} = \left.\frac{\partial v_2}{\partial y}\right|_{y=0} = 0 \tag{28}$$

The concentration of interfacial area in the mixture volume produced by the focusing system is defined as:

$$a_V = \frac{2h\overline{v}_s}{Q_1 + Q_2} \tag{29}$$

where

$$\overline{v}_s = \frac{2}{h}\int_0^{h/2} v_1(w_s/2, y)dy \tag{30}$$

represents the average interfacial velocity across the channel height.

Inspection of Eqs. (22)–(30) indicates that the ratio of the additive layer thickness to the channel width, w_s/w, depends on five dimensionless parameters. Four of these, F, P, ρ_2/ρ_1 and μ_2/μ_1, were already defined in the previous section. The fifth is the aspect ratio of the channel cross-section:

$$\alpha = h/w \tag{31}$$

With w_s/w determined, the ratio of the mean interfacial velocity to the mean channel velocity, $\overline{v}_s/\overline{v}$, can be calculated. This, in turn, allows the product of the interfacial area concentration and the channel hydraulic diameter to be expressed as:

$$a_V d_h = \frac{2h\overline{v}_s}{wh\overline{v}} \cdot \frac{2wh}{w+h} = \frac{4\alpha}{\alpha+1} \cdot \frac{\overline{v}_s}{\overline{v}} \tag{32}$$

The system of Eqs. (22)–(28), required to evaluate the additive layer thickness and interfacial area concentration, was solved using the FlexPDE 8.0 package. This software employs the finite element method with automatic unstructured mesh generation to handle partial differential equation systems (PDE Solutions Inc., 2025). The computational mesh is composed of triangular cells, within which cubic interpolation of solution variables is employed. The program estimates the relative uncertainty in the solution variables and compares this to an accuracy tolerance. If any mesh cell exceeds the tolerance, that cell is split, and the solution is recomputed. The mesh can be gridded more densely by the user. Tables 4 and 5 present the mesh independence test results for the upward flow of liquids with varying density and viscosity. The results indicate that when the number of mesh cells exceeds 5 700, the root-mean-square average of the error estimate over all cells (RMS error) remains below 0.01%. In subsequent calculations, meshes of this density were used.

Table 4. Effect of the number of grid cells on the width of the additive layer and interfacial surface concentration in the upward flow: $h/w = 1$, $F = 10$, $\rho_2/\rho_1 = 0.9$, $\mu_2/\mu_1 = 0.1$, $\varepsilon = 0.05$.

Number of cells	912	1486	5712	22216
w_s/w	0.051963	0.051963	0.051963	0.051963
$a_V d_h$	3.165954	3.165952	3.165953	3.165953
RMS error [%]	0.0295	0.0128	0.00305	0.00076

Table 5. Effect of the number of grid cells on the width of the additive layer and interfacial surface concentration in the upward flow: $h/w = 1$, $F = 10$, $\rho_2/\rho_1 = 1.1$, $\mu_2/\mu_1 = 10$, $\varepsilon = 0.05$.

Number of cells	948	1472	5712	22394
w_s/w	0.117821	0.117821	0.117821	0.117821
$a_V d_h$	1.570690	1.570689	1.570689	1.570689
RMS error [%]	0.00317	0.00198	0.000415	0.000076

To verify the correctness of the numerical calculations, their results were compared with experimental data available in the literature, including the experimental results reported by Giorello et al. (2020) in Fig. 5a. The results of this comparison, presented in Tables 6 and 7, indicate that the additive layer width predicted by the numerical model show good agreement with the experimental measurements.

Table 6. Comparison of the modelled additive layer width (this work) with the experimental results (Giorello et al., 2020) in the downward flow: $h/w = 0.058333$, $\rho_2/\rho_1 = 0.79$, $\mu_2/\mu_1 = 1.18$.

F	1.870	2.565	4.066	9.850
Re	0.9738	0.8735	0.7753	0.6876
$\sqrt{\text{Fr}}$	0.09837	0.08908	0.07986	0.07060
Experiment w_s/w	0.551	0.510	0.451	0.370
Model w_s/w	0.5530	0.5095	0.4508	0.3537

Table 7. Comparison of the modelled additive layer width (this work) with the experimental results (Giorello et al., 2020) in the downward flow: $h/w = 0.058333$, $\rho_2/\rho_1 = 1.15$, $\mu_2/\mu_1 = 1.4$.

F	1.618	2.219	2.731	4.137	8.597
Re	0.4202	0.3802	0.3628	0.3426	0.3333
$\sqrt{\text{Fr}}$	0.04059	0.03638	0.03426	0.03114	0.02800
Experiment w_s/w	0.232	0.171	0.151	0.111	0.081
Model w_s/w	0.2277	0.1723	0.1433	0.0992	0.0528

Subsequent modelling was carried out for various channel aspect ratios and liquids differing in density and with either equal or unequal viscosities, at a volumetric flow-rate ratio $F = 10$.

Figure 5 shows six representative velocity profiles in a square channel ($w = h$) for different density and viscosity ratios of the contacting liquids. The profiles were computed for upward flow with an axial pressure gradient close to the hydrostatic value ($\varepsilon = 0.05$). When the additive is both lighter and less viscous than the main stream ($\rho_2 < \rho_1$, $\mu_2 < \mu_1$), the velocity of the additive filament – and thus the interfacial velocity – is at its maximum (Fig. 5a). Equalising the additive viscosity with that of the focusing liquid lowers the centreline velocity (Fig. 5b). Further increasing the additive viscosity beyond that of the main stream produces a local depression in the velocity profile at the channel centre (Fig. 5c). Such a local minimum also appears whenever the additive is denser than the main stream ($\rho_2 > \rho_1$). The depression is most evident when the additive viscosity differs markedly – either lower or higher – from that of the focusing liquid (Figs. 5d and 5f). When the two viscosities are equal, the velocity profile remains relatively uniform at the channel centre (Fig. 5e).

The channel aspect ratio (h/w) is an additional factor that shapes the outcome of 2D focusing. Its effect on additive layer thickness is particularly evident at low ε across all vertical-flow cases (Fig. 6). A higher viscosity ratio amplifies this influence and extends it to regimes where gravitational effects are negligible ($\varepsilon \gg 1$). As with core–annular flow, when the additive is denser (lighter) than the main stream, the layer is thinner (thicker) in downward flow than in upward flow. Conversely, when the additive is lighter (denser), the thinner (thicker) layer appears in upward rather than downward flow. This contrast becomes more pronounced as ε approaches its minimum permissible value, below which the prescribed volumetric flow-rate ratio cannot be sustained. For upward flow (Figs. 6d–f), the effect of the density ratio on the normalised additive layer thickness is reversed relative to downward flow, while the overall shape of the w_s/w versus ε curves remains similar to that obtained for downward flow.

The most distinctive feature separating 2D from 3D hydrodynamic focusing is the extent of interfacial area development, which in 2D can be two to three times greater (Fig. 7) than in 3D focusing (Fig. 3). Moreover, the viscosity ratio influences the interfacial area concentration in a different and stronger way under 2D focusing. First, the effect is generally more pronounced than in 3D systems. Second, lowering the additive viscosity relative to the main stream markedly enhances the interfacial area concentration, even when $\varepsilon > 0.1$. Third, irrespective of the viscosity ratio, if the additive is denser (lighter) than the focusing liquid, the interfacial area concentration is higher (lower) in downward flow than in upward flow. Conversely, if the additive is lighter (denser), the concentration is higher (lower) in upward flow. As in core–annular flow, when ε approaches its minimum threshold values, the interfacial area concentration rapidly tends towards extremes. The steepest increase with decreasing ε occurs for downward flow with $\rho_2 > \rho_1$ or for upward flow with $\rho_2 < \rho_1$.

The influence of channel geometry and liquid density differences extends beyond changes in additive layer thickness and interfacial area concentration. The cross-sectional aspect ratio, h/w, also governs another key feature of 2D focusing flows – the residence time distribution (RTD) of the fluid elements. When product quality depends on process duration, for example the extent of reaction between the additive stream substrate and that in the focusing stream, it is desirable to minimise the spread of residence times of additive stream elements. To this end, RTD density functions E were calculated for two channel aspect ratios, $w/h = 0.1$ and 10.

The dimensionless RTD density functions for both liquids were estimated using:

$$E_i(\theta) \cong \frac{1}{\Delta\theta Q_i} \sum_j Q_{i,j}, \quad i = 1, 2 \tag{33}$$

The dimensionless residence time θ was defined as the ratio of the mean velocity of the i-th liquid in the channel to its local velocity:

$$\theta = \frac{\overline{v}_i}{v_i} \tag{34}$$

The summation of the partial volumetric flow rates $Q_{i,j}$ was carried out over computational grid elements for which the mean velocity satisfied:

$$\theta - \frac{1}{2}\Delta\theta \leqslant \frac{\overline{v}_i}{\overline{v}_{i,j}} < \theta - \frac{1}{2}\Delta\theta \tag{35}$$

where $\Delta\theta$ denotes the time step used in the calculations.

The computed RTDs for downward flow of liquids with different densities and viscosities are shown in Fig. 8. For $h/w = 10$, the RTD of the main stream closely resembles that of laminar single-liquid channel flow: a sharp rise to a maximum at $\theta \approx 0.5$, followed by a gradual decline towards zero before $\theta \approx 3$ (Figs. 8a, 8c). Reducing the aspect ratio to 0.1 broadens the distribution at short residence times, most notably when the additive is denser than the main stream. The most striking differences, however, appear in the RTD of the additive stream. With $h/w = 10$, the E function exhibits a narrow peak around $\theta \approx 1$ (Figs. 8b, 8d), indicative of a very tight residence-time distribution characteristic of plug-like flow. By contrast, when the channel width greatly exceeds its height ($h/w = 0.1$), hydrodynamic focusing effectively occurs under Hele–Shaw flow conditions. This results in substantial flattening and broadening of the RTD over $\theta \approx 0.5$–1.5, irrespective of the density ratio of the two liquids.

An additional consequence of Hele–Shaw flow focusing is a drastic reduction in interfacial area concentration. This key parameter for mass transfer decreases from $a_V = 5.29/d_h$ to $0.39/d_h$ for $\rho_2/\rho_1 = 0.9$, and from $a_V = 5.54/d_h$ to $0.64/d_h$ for $\rho_2/\rho_1 = 1.1$, when the aspect ratio w/h is reduced by two orders of magnitude from 10 to 0.1.

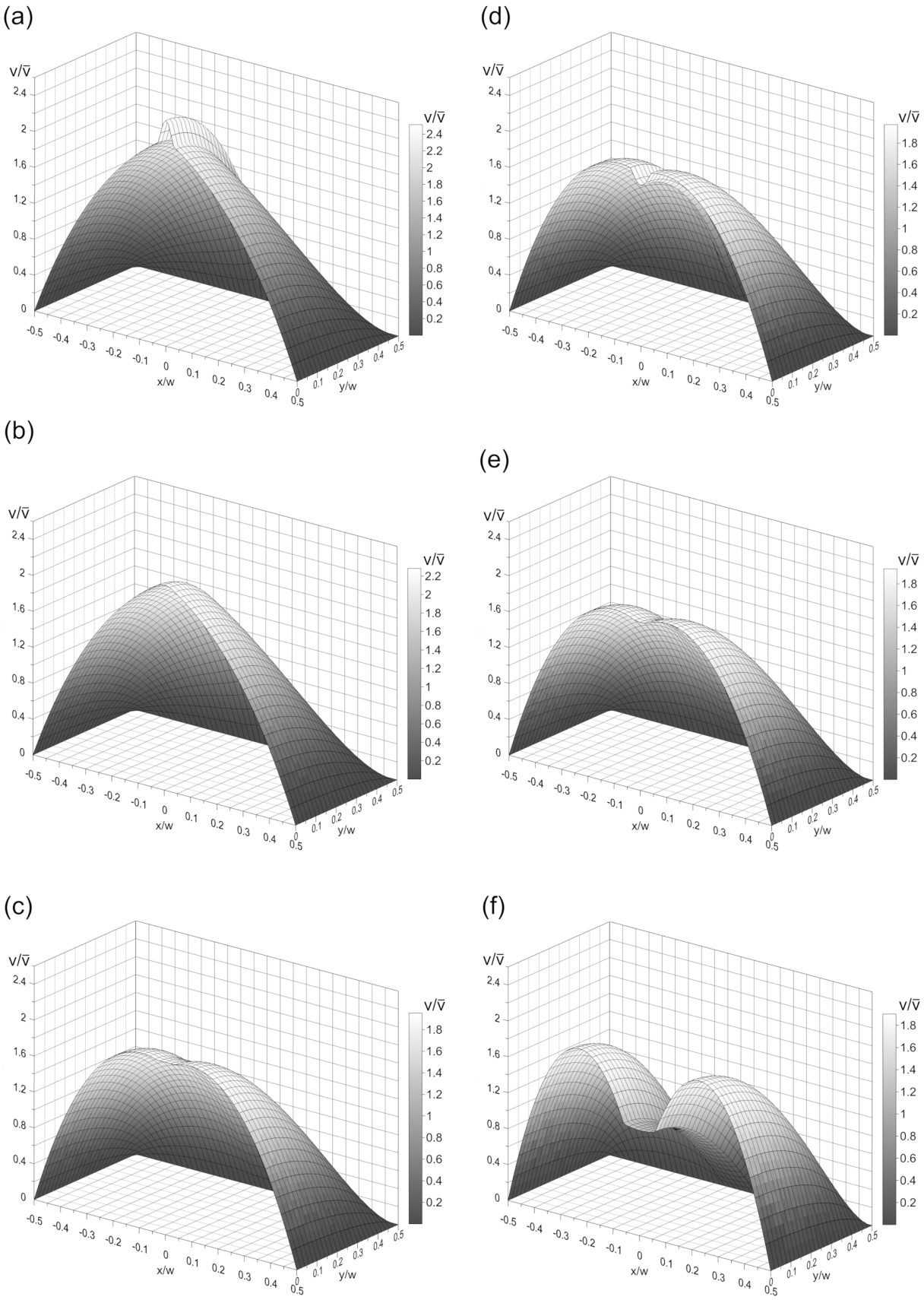

Figure 5. Velocity profiles in upward stratified flow under 2D hydrodynamic focusing ($F = 10$) for different density and viscosity ratios: (a) $\rho_2/\rho_1 = 0.9$ and $\mu_2/\mu_1 = 0.1$, (b) $\rho_2/\rho_1 = 0.9$ and $\mu_2/\mu_1 = 1$, (c) $\rho_2/\rho_1 = 0.9$ and $\mu_2/\mu_1 = 10$, (d) $\rho_2/\rho_1 = 1.1$ and $\mu_2/\mu_1 = 0.1$, (e) $\rho_2/\rho_1 = 1.1$ and $\mu_2/\mu_1 = 1$, (f) $\rho_2/\rho_1 = 1.1$ and $\mu_2/\mu_1 = 10$.

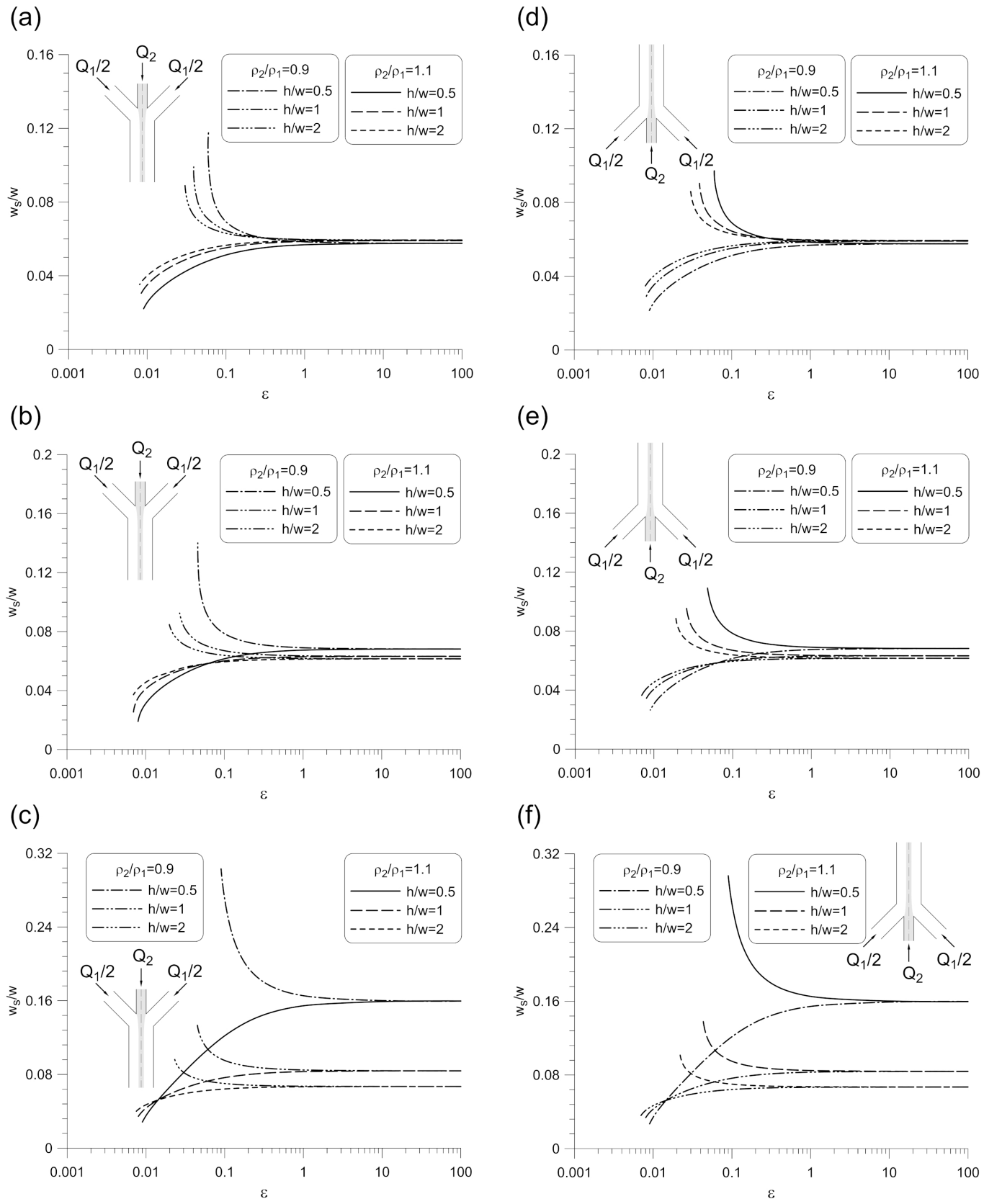

Figure 6. Influence of density ratio, viscosity ratio, and channel aspect ratio on the normalised thickness of the additive layer in vertical stratified flow ($F = 10$): (a) downward flow, $\mu_2/\mu_1 = 0.1$; (b) downward flow, $\mu_2/\mu_1 = 1$; (c) downward flow, $\mu_2/\mu_1 = 10$; (d) upward flow, $\mu_2/\mu_1 = 0.1$; (e) upward flow, $\mu_2/\mu_1 = 1$; (f) upward flow, $\mu_2/\mu_1 = 10$.

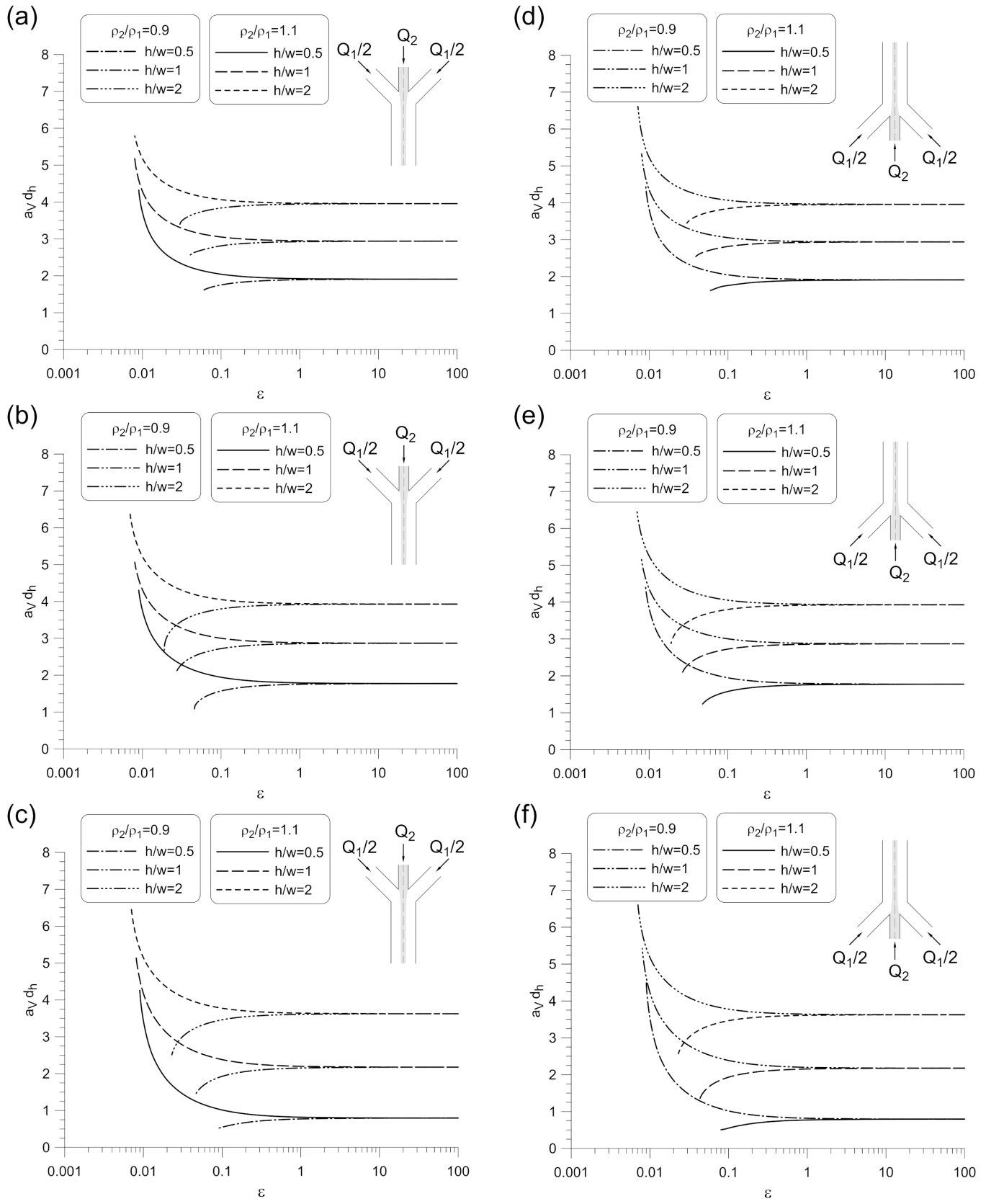

Figure 7. Influence of density ratio, viscosity ratio, and channel aspect ratio on the normalised interfacial area concentration in vertical stratified flow ($F = 10$): (a) downward flow, $\mu_2/\mu_1 = 0.1$; (b) downward flow, $\mu_2/\mu_1 = 1$; (c) downward flow, $\mu_2/\mu_1 = 10$; (d) upward flow, $\mu_2/\mu_1 = 0.1$; (e) upward flow, $\mu_2/\mu_1 = 1$; (f) upward flow, $\mu_2/\mu_1 = 10$.

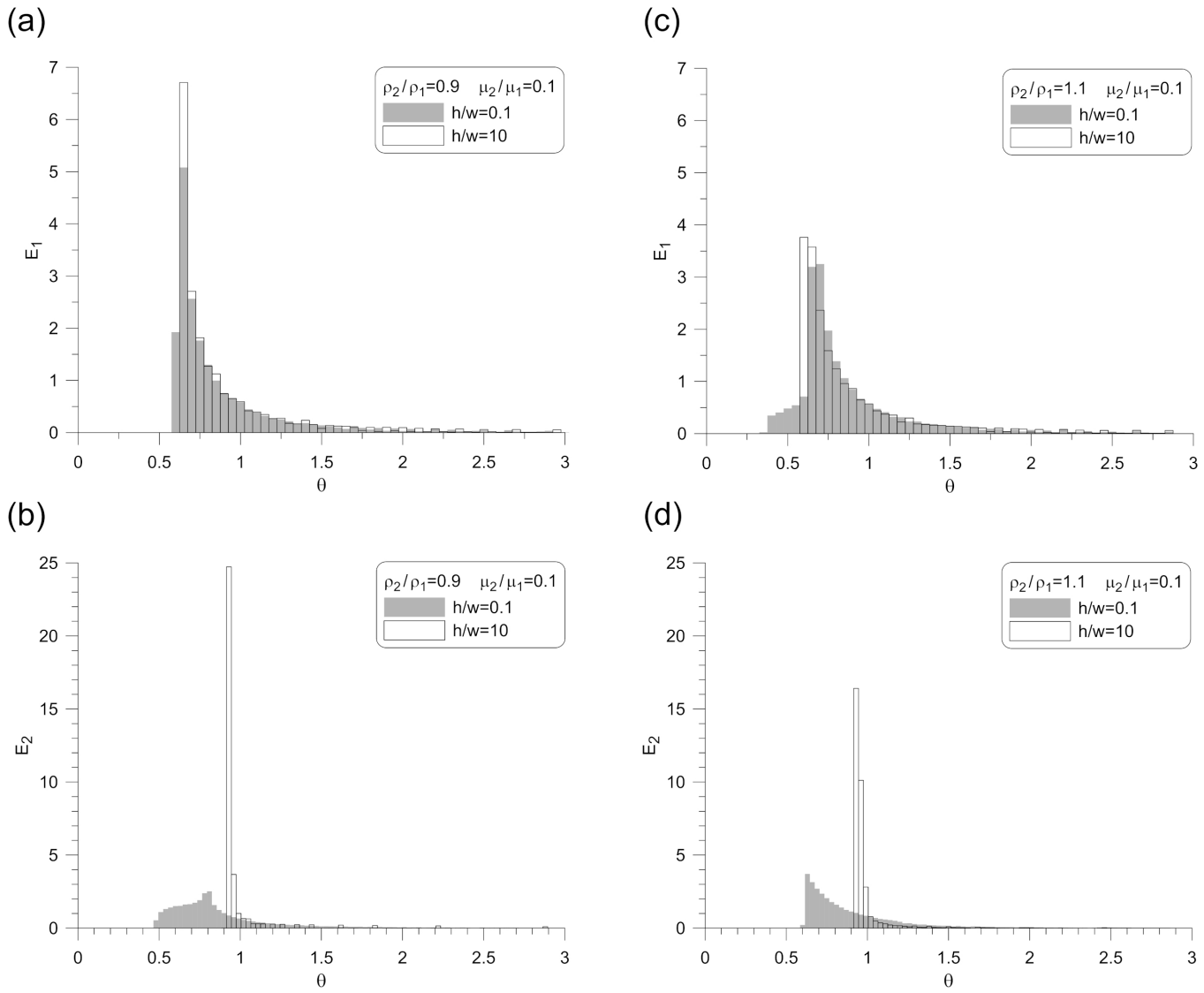

Figure 8. Influence of channel aspect ratio and density ratio on the residence-time distribution (RTD) function in vertical stratified downward flow ($F = 10$, $\mu_2/\mu_1 = 0.1$, $\varepsilon = 0.1$): (a) focusing stream, $\rho_2/\rho_1 = 0.9$; (b) additive stream, $\rho_2/\rho_1 = 0.9$; (c) focusing stream, $\rho_2/\rho_1 = 1.1$; (d) additive stream, $\rho_2/\rho_1 = 1.1$.

3. CONCLUSIONS

This work has demonstrated how hydrodynamic focusing in vertical channels governs the geometry of the additive stream and the development of liquid–liquid interfacial area. Two canonical system configurations were examined: axisymmetric core–annular flow in a circular channel (3D focusing) and symmetric stratified flow in a rectangular channel (2D focusing).

In the case of 3D focusing, analytical solutions of the Navier–Stokes equations showed that the radius of the additive filament and the extent of interfacial development are strongly influenced by density differences between the contacting liquids, particularly when the axial pressure gradient approaches the hydrostatic pressure gradient. Viscosity ratio played a secondary role, modifying but not dominating the final outcome.

Numerical simulations of 2D focusing flow revealed that the additive layer thickness and interfacial area concentration depend not only on density and viscosity contrasts but also on the channel aspect ratio. These effects were especially pronounced under near-hydrostatic pressure gradients. Compared with the core–annular case, 2D focusing consistently produced a higher degree of interfacial area development, highlighting its potential as a more effective method for enhancing mass transfer. The analysis of residence-time distributions further demonstrated that appropriate aspect ratios are required to minimise dispersion of the additive stream, thereby improving mixing uniformity.

The conclusions drawn in this study are restricted to stable, fully developed laminar focusing regimes, for which hydrodynamic instabilities do not arise and the flow assumptions underlying the analytical and numerical models remain valid.

Within this regime, the results provide quantitative benchmarks for how liquid properties and channel geometry determine the outcome of hydrodynamic focusing.

From an application viewpoint, the results indicate that vertical hydrodynamic focusing can be effective in continuous flow systems in generation of intermaterial surface area, provided that precise and uniform dosing of both streams is ensured and that the pressure gradient is carefully controlled relative to the hydrostatic pressure contribution.

Although the present study was restricted to the overall outcome of 2D and 3D focusing under different operating conditions, without attempting to resolve the detailed dynamics of the focusing process, the results provide clear benchmarks for how liquid properties and channel geometry determine the outcome of hydrodynamic focusing. Extending the analysis beyond the stable laminar flow requires a dedicated stability-focused investigation to identify the onset and nature of interfacial instabilities. Such an analysis constitutes a necessary next step before the present framework can be applied to unstable or transitional flow conditions.

The findings of this study thus provide a useful basis for more advanced CFD investigations of liquid–liquid systems differing in density and viscosity under vertical flow conditions.

ACKNOWLEDGEMENTS

The research has been financed from statutory funds of the Warsaw University of Technology, Poland.

SYMBOLS

A	channel cross-sectional area, m^2
a_V	interfacial area concentration, 1/m
d_h	hydraulic diameter, 1/m
E	residence time distribution function
Eu	Euler number
F	ratio of volumetric flow rates
Fr	Froude number
g	gravitational acceleration, m/s^2
h	channel height, m
L	channel length, m
P	pressure modulus defined by Eq. (14)
p	pressure, Pa
$\tilde{p}$	modified pressure, Pa
Q_i	total volumetric flow rate of the i-th liquid, m^3/s
$Q_{i,j}$	volumetric flow rate of the i-th liquid in the j-th grid cell, m^3/s
R	channel radius, m
Re	Reynolds number
r	radial coordinate, m
r_s	radius of the focused stream, m
w	channel width, m
w_s	width of the focused stream, m
v_i	axial velocity of the i-th liquid, m/s
$v_{i,j}$	axial velocity of the i-th liquid in j-th grid cell, m/s
v_s	liquid velocity at the liquid-liquid interface, m/s
xy, z	cartesian coordinates, m

Greek symbols

α	channel aspect ratio
ε	dimensionless parameter
θ	dimensionless residence time
μ	liquid viscosity, kg/(m·s)
ρ	liquid density, kg/m^3

Subscripts

1	focusing liquid (main stream)
2	focused liquid (additive stream)
min	minimum value

Special symbols

$\bar{}$	mean

REFERENCES

Aref H., 1984. Stirring by chaotic advection. *J. Fluid Mech.*, 143, 1–21. DOI: 10.1017/S0022112084001233.

Bałdyga J., Rożeń A., 1994. Investigation of micromixing in very viscous liquids. *8th European Conference of Mixing*, Cambridge, UK, 21–23 September 1994, 267–274.

Bothe D., Stemich C., Warnecke H.-J., 2008. Computation of scales and quality of mixing in a T-shaped microreactor. *Comput. Chem. Eng.*, 32, 108–114. DOI: 10.1016/j.compchemeng.2007.08.001.

Chen Y., Wu L., Zhang L., 2015. Dynamic behaviors of double emulsion formation in a flow-focusing device. *Int. J. Heat Mass Transfer*, 82, 42–50. DOI: 10.1016/j.ijheatmasstransfer.2014.11.027.

Chiu Y.-J., Cho S.H., Mei Z., Lien V., Wu T.-F., Lo Y.-H., 2013. Universally applicable three-dimensional hydrodynamic microfluidic flow focusing. *Lab Chip*, 13, 1803–1809. DOI: 10.1039/c3lc41202d.

Cubaud T., Mason T.G., 2008. Capillary threads and viscous droplets in square microchannels. *Phys. Fluids*, 20, 053302. DOI: 10.1063/1.2911716.

Cubaud T., Notaro S., 2014. Regimes of miscible fluid thread formation in microfluidic focusing sections. *Phys. Fluids*, 26, 122005. DOI: 10.1063/1.4903534.

Dziubinski M., 2012. Hydrodynamic focusing in microfluidic devices. In: Kelly R.T. (Ed.), *Advances in microfluidics*. IntechOpen, 2012, 29–54. DOI: 10.5772/34690.

Gao Y., Zhu D.F., Han Y., Torrente-Murciano L., 2021. Rational design of the inlet configuration of flow systems for enhanced mixing. *J. Flow. Chem.*, 11, 589–598. DOI: 10.1007/s41981-021-00184-z.

Giorello A., Minetti F., Nicastro A., Berli C.L.A., 2020. The effect of gravity on microfluidic flow focusing. *Sens. Actuators B: Chem.*, 307, 127595. DOI: 10.1016/j.snb.2019.127595.

Golden J.P., Justin G.A., Nasir M., Ligler F.S., 2012. Hydrodynamic focusing – a versatile tool. *Anal. Bioanal. Chem.*, 402, 325–335. DOI: 10.1007/s00216-011-5415-3.

Heravi P., Chu L.-A., Yao D.-J., 2023. An empirical model for lateral flow in horizontally stratified flows. *Microfluid. Nanofluid.*, 27, 4. DOI: 10.1007/s10404-022-02612-5.

Hessel V., Löwe H., Schönfeld F., 2005. Micromixers – a review on passive and active mixing principles. *Chem. Eng. Sci.,* 60, 2479–2501. DOI: 10.1016/j.ces.2004.11.033.

Huyke D.A., Ramachandran A., Oyarzun D.I., Kroll T., DePonte D.P., Santiago J.G., 2020. On the competition between mixing rate and uniformity in a coaxial hydrodynamic focusing mixer. *Anal. Chim. Acta*, 1103, 1–10. DOI: 10.1016/j.aca.2020.01.013.

Jaffer S.A., Wood P.E., 1998. Quantification of laminar mixing in the Kenics static mixer: an experimental study. *Can. J. Chem. Eng.*, 76, 516–521. DOI: 10.1002/cjce.5450760323.

Joseph D.D., Renardy Y.Y., 1993. *Fundamentals of two-fluid dynamics. Part II: Lubricated transport, drops and miscible liquids*. Springer New York. DOI: 10.1007/978-1-4615-7061-5.

Karnik R., Gu F., Basto P., Cannizzaro C., Dean L., Kyei-Manu W., Langer R., Farokhzad O.C., 2008. Microfluidic platform for controlled synthesis of polymeric nanoparticles. *Nano Lett.*, 8, 2906–2912. DOI: 10.1021/nl801736q. DOI:

Kennedy M.J., Stelick S.J., Sayam L.G., Yen A., Erickson D., Batt C.A., 2011. Hydrodynamic optical alignment for microflow cytometry. *Lab Chip*, 11, 1138–1143. DOI: 10.1039/c0lc00500b.

Knight J.B., Vishwanath A., Brody J.P., Austin R.H, 1998. Hydrodynamic focusing on a silicon chip: mixing nanoliters in microseconds. *Phys. Rev. Lett.*, 80, 3863–3866. DOI: 10.1103/PhysRevLett.80.3863.

Knoška J., Adriano L., Awel S., Beyerlein K.R., Yefanov O., Oberthuer D., Peña Murillo G.E., Roth N., Sarrou I., Villanueva-Perez P., Wiedorn M.O., Wilde F., Bajt S., Chapman H.N., Heymann M., 2020. Ultracompact 3D microfluidics for time-resolved structural biology. *Nat. Commun.*, 11, 657. DOI: 10.1038/s41467-020-14434-6.

Lee G.-B., Chang C.-C., Huang S.-B., Yang R.-J., 2006. The hydrodynamic focusing effect inside rectangular microchannels. *J. Micromech. Microeng.*, 16, 1024–1032, DOI: 10.1088/0960-1317/16/5/020.

Lu M., Ho Y.-P., Grigsby C.L., Nawaz A.A., Leong K.W., Huang T.J., 2014. Three-dimensional hydrodynamic focusing method for polyplex synthesis. *ACS Nano*, 8, 332–339. DOI: 10.1021/nn404193e.

Lu M., Ozcelik A., Grigsby C.L., Zhao Y., Guo F., Leong K.W., Huang T.J., 2016. Microfluidic hydrodynamic focusing for synthesis of nanomaterials. *Nano Today*, 11, 778–792. DOI: 10.1016/j.nantod.2016.10.006.

Mansur E.A., Ye M., Wang Y., Dai Y., 2008. A state-of-the-art review of mixing in microfluidic mixers. *Chin. J. Chem. Eng.,* 16, 503–516. DOI: 10.1016/S1004-9541(08)60114-7.

Metzner A.B, Reed J.C., 1955. Flow of non-newtonian fluids – correlation of the laminar, transition, and turbulent – flow regions. *AIChE J.*, 1, 434–440. DOI: 10.1002/aic.690010409.

Minetti F., Giorello A., Olivares M.L., Berli C.L.A., 2020. Exact solution of the hydrodynamic focusing driven by hydrostatic pressure. *Microfluid. Nanofluid.*, 24, 15. DOI: 10.1007/s10404-020-2322-y.

Minetti F., Mengatto L.N., Olivares M.L., Berli C.L.A., 2022. Generation of curcumin-loaded albumin nanoparticles by using off-the-shelf microfluidics driven by gravity. *Food Res. Int.*, 162, 111984. DOI: 10.1016/j.foodres.2022.111984.

Ottino J.M., 1989. *The kinematics of mixing: stretching, chaos, and transport*. Cambridge University Press.

Ottino J.M., Ranz W.E., Macosko C.W., 1979. A lamellar model for analysis of liquid-liquid mixing. *Chem. Eng. Sci.*, 34, 877–890. DOI: 10.1016/0009-2509(79)85145-3.

PDE Solutions Inc., 2025. *FlexPDE 8 User Manual*. Available at: https://www.pdesolutions.com/user-manuals/.

Press W.H., Teukolski S.A., Vetterling W.T., Flannery B.P., 1992. *Numerical recipes in C: The art of scientific computing*. 2nd edition, Cambridge University Press, Cambridge.

Rahbarshahlan S., Bakhshayesh A.G., Khosroshahi A.R., Aligholami M., 2021. Interface study of the fluids in passive micromixers by altering the geometry of inlets. *Microsyst. Technol.,* 27, 2791–2802. DOI: 10.1007/s00542-020-05067-2.

Rożeń A., Kopytowski J., 2021. Energetic efficiency of mixing in a periodically reoriented Dean flow. *Chem. Proc. Eng.,* 42, 391–410. DOI: 10.24425/cpe.2021.138937.

Rożeń A., Kopytowski J., 2025. Application of the volume of fluid method to calculate the intermaterial surface area density created in different focusing flow configurations. *Chem. Eng. Res. Des.*, 217, 189–205. DOI: 10.1016/j.cherd.2025.03.033.

Shivhare P.K., Bhadra A., Sajeesh P., Prabhakar A., Sen A.K., 2016. Hydrodynamic focusing and interdistance control of particle-laden flow for microflow cytometry. *Microfluid. Nanofluid.*, 20, 86. DOI: 10.1007/s10404-016-1752-z.

Stiles P.J., Fletcher D.F., 2003. Effects of gravity on the steady state of a reaction in a liquid-state microreactor – deviations from Poiseuille flow. *Phys. Chem. Chem. Phys.*, 5, 1219–1224. DOI: 10.1039/b211686c.

Stiles P.J., Fletcher D.F., 2004. Hydrodynamic control of the interface between two liquids flowing through a horizontal or vertical microchannel. *Lab Chip*, 4, 121–124. DOI: 10.1039/b315524b.

Tripathi S., Chakravarty P., Agrawal A., 2014. On non-monotonic variation of hydrodynamically focused width in a rectangular microchannel. *Curr. Sci.*, 107, 1260–1274.

Weigl B.H, Kriebel J., Mayes K.J., Bui T., Yager P., 1999. Whole blood diagnostics in standard gravity and microgravity by use of microfluidic structures (T-Sensors). *Mikrochim. Acta*, 131, 75–83. DOI: 10.1007/s006040050011.

Wu T., Luo Z., Ding W., Cheng Z., He L., 2017. Monodisperse droplets by impinging flow-focusing. *Microfluid. Nanofluid.*, 21, 129. DOI: 10.1007/s10404-017-1966-8.

Yamada H., Yoshida Y., Terada N., Hagihara S., Komatsu T., Terasawa A., 2008. Fabrication of gravity-driven microfluidic device. *Rev. Sci. Instrum.*, 79, 124301. DOI: 10.1063/1.3030859.

Yamaguchi Y., Honda T., Briones M.P., Yamashita K., Miyazaki M., Nakamura H., Maeda H., 2006. Influence of gravity on a laminar flow in a microbioanalysis system. *Meas. Sci. Technol.*, 17, 3162–3166. DOI: 10.1088/0957-0233/17/12/S07.

Zhang H., Kopfmüller T., Achermann R., Zhang J., Teixeira A., Shen Y., Jensen K.F., 2019. Accessing multidimensional mixing via 3D printing and showerhead micromixer design. *AIChE J.*, 66, e16873. DOI: 10.1002/aic.16873.

Zlokarnik M., 2001. *Stirring. Theory and practice.* Wiley-VCH Verlag GmbH, Weinheim. DOI: 10.1002/9783527612703.